Applied Surface Science 587 (2022) 152861

Contents lists available at ScienceDirect

Applied Surface Science

journal homepage: www.elsevier.com/locate/apsusc

Full Length Article

Thermally sprayed MCO/FeCr24 interconnector with improved stability for tubular segmented-in-series SOFCs

Yingzhen Hu [a,b], Jiu-Tao Gao [b], Cheng-Xin Li [b,*], Chang-Jiu Li [b]

[a] College of Metallurgical Engineering, Xi'an University of Architecture and Technology, Xi'an 710055, Shaanxi, PR China
[b] State Key Laboratory for Mechanical Behavior of Materials, School of Materials Science and Engineering, Xi'an Jiaotong University, Xi'an, Shaanxi 710049, PR China

ARTICLE INFO

Keywords:
Thermal spraying
$Mn_{1.5}Co_{1.5}O_4$ spinel coating
FSS interconnector
Tubular segmented-in-series SOFC

ABSTRACT

The present work aims to evaluate the feasibility of thermally sprayed $Mn_{1.5}Co_{1.5}O_4$/FeCr24 interconnect under real operating environment of tubular solid oxide fuel cells (SOFC). Different from the planar SOFC, further practical application of ferritic stainless steels interconnector is still limited in tubular SOFC, mainly due to the special construction and complex operating environment. Investigating the stability of interconnector under reducing-oxidizing (redox) atmosphere is an important issue towards practical applications of tubular SOFC. In this work, thermal spraying was applied as a cost-effective method to prepare the segmented-in-series SOFCs based on $Mn_{1.5}Co_{1.5}O_4$/FeCr24 interconnector. The detailed heating and deposition process for different $Mn_{1.5}Co_{1.5}O_4$ particles, quantitative relationship between the $Mn_{1.5}Co_{1.5}O_4$ coating thickness (δ_0) and microstructure homogenization rate ($d\delta/dt$) during oxidizing treatment, as well as the feasibility of thermally-sprayed $Mn_{1.5}Co_{1.5}O_4$/FeCr24 interconnect for tubular SOFC applications in range of 600–800 °C were thoroughly evaluated.

1. Introduction

As a clean and efficient energy conversion device, solid oxide fuel cells (SOFC) represents one of the most potential power generation systems owing to their fuel flexibility and high system efficiencies [1–5]. To produce a usable power output, multiple single fuel cells are usually stacked in electrical series via interconnectors. As a key component in SOFC stacks, the interconnector electrically connects the adjacent single cells while physically separating the fuel from the oxidant gas. In planar SOFC systems, the interconnectors are generally designed in form of bulk materials and exposed only to the oxidizing atmosphere. While for tubular types, many systems with high efficiency and high stability have been developed using the "segmented-in-series" SOFC (SS-SOFC) design, with the cells delineated in bands around the tube [6–9]. In this design, the cell components (anode/electrolyte/cathode/interconnector) are deposited layer by layer onto the porous tube, and then one end of the tube is sealed. During the stack operation, the fuel/oxidant gas is transported inside the tube by a feeding pipe and released near the closed end of the cell, while the oxidant/fuel gas is transmitted outside the tube in opposite direction. In the whole process, the interconnector is exposed to both anodic reducing (H_2) and cathodic oxidation (O_2) atmospheres simultaneously. As a result, good chemical, microstructural, and phase stabilities for the interconnector are required in both the reducing and oxidizing environments (redox condition).

To render SOFC technology economically feasible, both their fabricating cost and the operating temperature need to be further decreased. Developing intermediate-temperature (600–800 °C) tubular SOFCs through low-cost manufacturing process is the critical step towards commercialization. In recent years, thermal spraying (TS) characterized with high deposition rate, high automation, high flexibility and low cost have been used for the manufacturing of tubular SOFCs, such as Siemens Westinghouse Power Corporation (SWH) and Mitsubishi Heavy Industries (MHI) stacks [10–14]. The output power for our thermally sprayed tubular SS-SOFC stacks assembled with 56 tubes (ten cells in series per tube) reached more than 800 W at 830 °C, indicating a promising potential of TS technology for large-scale power generation application [15]. On the other side, progresses in the intermediate-temperature (600–800 °C) SOFCs have facilitated the application of less expensive metallic interconnectors [16,17]. Due to the excellent electric performance, good thermal compatibility, high impact-resistance, and low fabrication cost, Cr-containing ferritic stainless steels (FSS) such as Crofer 22 APU [18,19], Crofer 22H [20,21], T441

* Corresponding author.
E-mail addresses: yzhu@xauat.edu.cn (Y. Hu), gaojiutao@xjtu.edu.cn (J.-T. Gao), licx@mail.xjtu.edu.cn (C.-X. Li), licj@mail.xjtu.edu.cn (C.-J. Li).

https://doi.org/10.1016/j.apsusc.2022.152861
Received 18 November 2021; Received in revised form 12 February 2022; Accepted 15 February 2022
Available online 24 February 2022

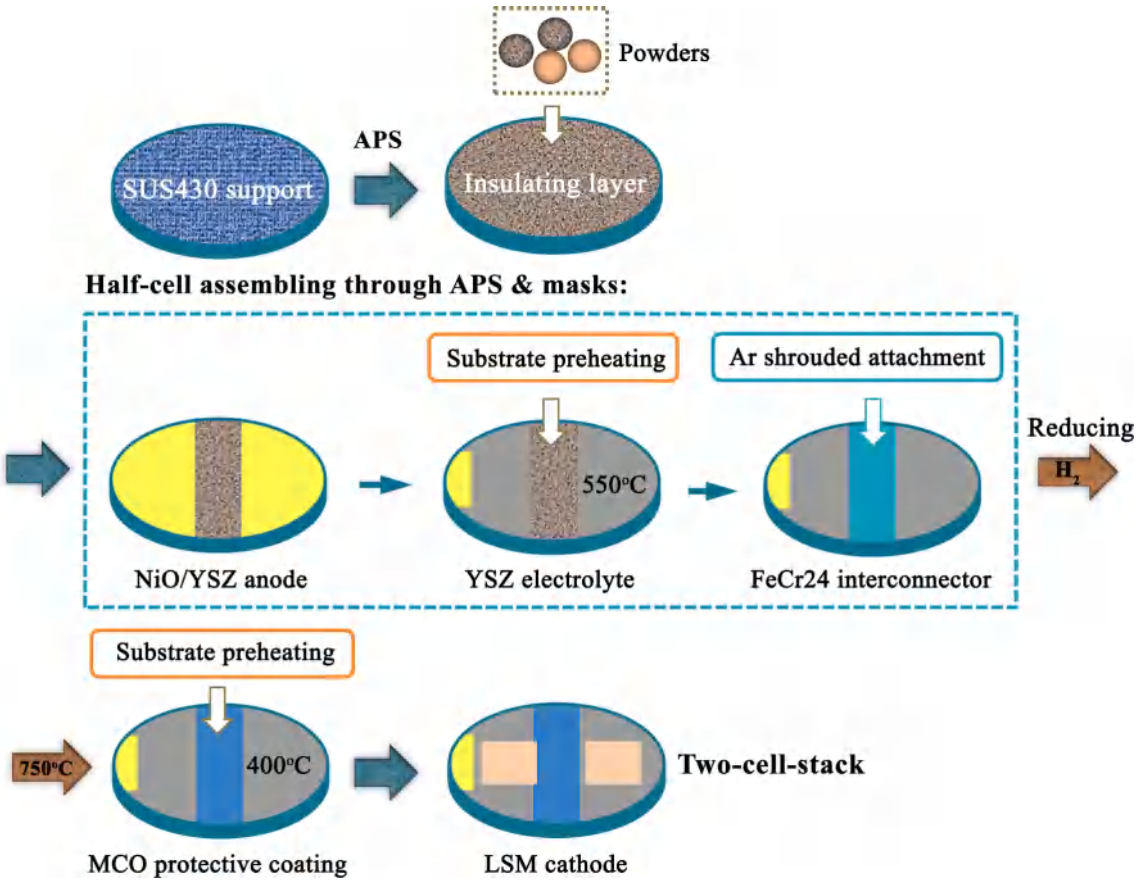

Fig. 1. Manufacturing scheme of current thermally sprayed two-cell-stack assembled with MCO/FeCr24 interconnector.

[22–24], and SUS430 [25,26] have been developed as promising interconnector materials for SOFC stacks. However, the typical cathode operating environment inevitably causes the formation of Cr-rich oxide layers at the cathode/interconnector interface, which could grow linearly in term of square root of the operation time [27,28]. The continuous scale growth may lead to adverse consequences as follows: (i) increased electrical resistance and possibility of coating spallation, which would be further exacerbated by the thermal mismatch between the oxide layer and substrate; (ii) accelerated volatilization of Cr^{6+} species (e.g. CrO_3, $CrO_2(OH)_2$) [29] at the three-phase boundary and then drastic cell performance degradation [30,31]. It was suggested that a dense outer scale such as $(Cr,Mn)_3O_4$, $(Cr,Mn,Fe)_3O_4$ could be generated in prior to the formation of Cr_2O_3 layer, and then reduce the Cr evaporation rate to some extent, by adding elements with high oxygen affinity (e.g. Mn, Ti) into the FSS substrates [32,33]. Crofer 22 APU and similar alloys specifically developed for SOFC stacks exhibited good performance in real stack tests [18,34]. Nevertheless, these special interconnectors are rather expensive and unattractive for commercial applications, in comparison to commodity FSS such as T441 and SUS430. Moreover, the stack performance degradation caused by Cr-poisoning is still considerable. To effectively prevent Cr-volatilization and improve the stack performance stability, application of long-term stable protective coatings over the interconnector is indispensable.

To date, Mn-Co based spinel, Mn-Cu based spinel [35,36], Fe-containing spinel such as $NiFe_2O_4$ [37], $CuFe_2O_4$ [38], and $(Fe,Co,Ni)_3O_4$ [39] have exhibited promising potential for SOFC interconnects. Among variety of materials, $(Mn,Co)_3O_4$ coatings including $Mn_{1.5}Co_{1.5}O_4$ [40,41], $MnCo_2O_4$ [21], Fe-doped [42] and Cu-doped [43] Mn-Co spinels have evoked great interest, owing to their satisfactory electrical conductivity, well-matched thermal properties, and especially the efficiency in retarding oxygen transfer and inhibiting Cr-vaporization. The spinel coatings have been deposited by various techniques such as thermal spraying [44,45], electrodeposition [46–48], magnetron sputtering [49], screen printing [43], and slurry spraying [50]. By adopting substrate-preheating strategy, rather dense $Mn_{1.5}Co_{1.5}O_4$ (MCO) coatings were successfully deposited onto the planar T441 interconnector through atmospheric plasma spray (APS) technology without any post-treatments. The APS-MCO coatings with high structural stability effectively improved the oxidation resistance of the interconnector during long-term operation under the SOFC cathode environment [40]. Based on the reduction–oxidation properties of Mn-Co oxide spinel, Gao et al. [51] also realized improved performance for thermally-sprayed planar SOFCs assembled with MCO/$La_{0.6}Sr_{0.4}Co_{0.2}Fe_{0.8}O_3$ (LSCF) current collector. The long-term stack testing (nearly 35,000 h) conducted by Forschungszentrum Jülich showed very low chromium evaporation into the cathode, indicating the great effectiveness of Mn-Co-Fe spinel coated interconnector for planar SOFCs [52]. However, the further practical application of FSS interconnector in tubular SOFCs is still limited by several issues: (i) bulk stainless steel is not suitable for the interconnector, based on the specific structure and fabrication process of tubular SOFCs; (ii) the tubular designs set much stricter requirements in the microstructural stability, phase composition, and electrical properties for the interconnector, which operates under both the anodic reducing and cathodic oxidation atmospheres (redox atmosphere). Therefore, investigating the behavior of interconnector/protective coating systems under redox condition is an important issue towards practical applications of tubular SOFCs for long-term operation.

Our basic objective in current work is to evaluate the feasibility of FSS interconnector layers under the real operating environment of tubular segmented-in-series SOFCs. First, the heating and deposition models for MCO particles under different states were proposed, based on

Table 1
Spray processing parameters for current two-cell-stack.

Coatings	Arc current (A)	Arc power (kW)	Spray distance (mm)	Traverse speed (mm·s^{-1})	Ar (slpm)	H_2 (slpm)	N_2 (slpm)
MgO-Al_2O_3	600	36	80	400	40	5	6
NiO-YSZ	600	36	80	600	45	5	5
8YSZ	600	42	80	600	45	6	5
FeCr24	600	36	140	600	43.5	4.5	6
MCO	600	36	80	600	45	6	5
LSM	600	30	80	600	45	5	5

the monitoring results of inflight particle temperature and as-spraying coatings. Then MCO coatings with different thickness (10 μm, 40 μm, 100 μm) were exposed to isothermal oxidation at 800 °C for different durations (10 h, 30 h, 50 h, 100 h, 300 h), aiming to construct a quantitative characterization on the microstructure homogenization rate ($d\delta/dt$), and determine a feasible coating thickness for the stack operation. Afterwards, plasma sprayed $Mn_{1.5}Co_{1.5}O_4$/FeCr24 interconnector was exposed to Air/H_2 redox atmosphere at 800 °C for 120 h, in order to evaluate the phase, structural, and electrical stabilities under simulating conditions of tubular cells. Ultimately, two cells in series were deposited onto SUS430 porous support and tested under real operating environment of tubular SOFCs, to examine the output performance and microstructure stability.

2. Experimental

2.1. Fabrication of the segmented-in-series SOFC

Two thermally sprayed cells with an effective electrode area (active area) of 3.4 cm^2 were deposited on the porous SUS430 support and connected in series through MCO/FSS interconnector with length of 8 mm. The porous steel support in thickness of 1.2 mm demonstrates an apparent porosity of 17.7% and high gas permeability of 1.07 × 10^{-2} cm^4 gf^{-1}·s^{-1}, which could provide enough through-thickness pores for fuel gas diffusion. During the cell fabrication, six spray powders were utilized and the detailed morphologies are presented in Fig. S1. Commercial MgO-Al_2O_3 (1.6:1 wt%) composite powders provided by Yiyang Xiandao plasma spray powder company were used for the insulating layer, with a particle size of 45–75 μm. Commercial agglomerated $La_{0.8}Sr_{0.2}MnO_3$ (LSM, 10–30 μm, Fujimi), NiO-YSZ (10–25 μm, Qingdao Tianyao) powders, and 8 mol.%Y_2O_3-ZrO_2 fuse-crushed powder (8YSZ,

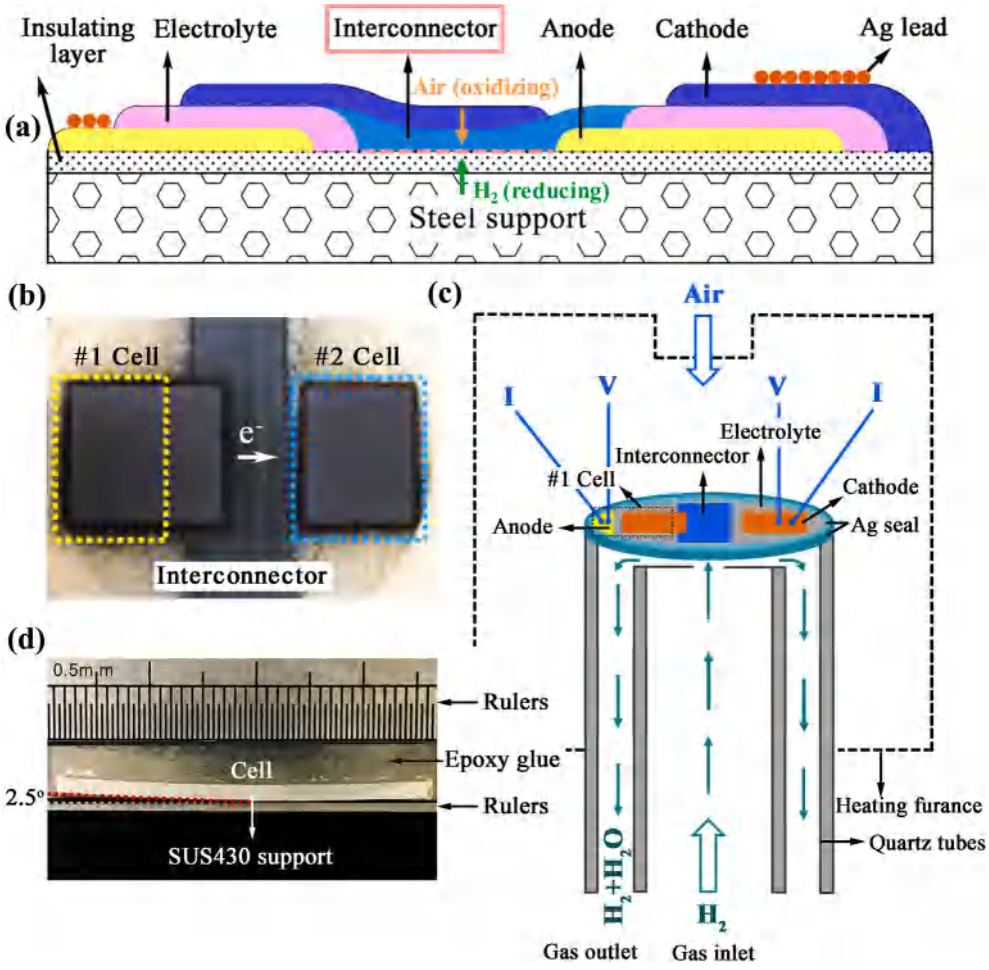

Fig. 2. Thermally sprayed segmented-in-series SOFC sub-module assembled with MCO/FeCr24 interconnector: (a) the structure diagram; (b) photo of a two-cell-stack; (c) diagram of the output performance testing assembly; and (d) cutting section from the tested cells.

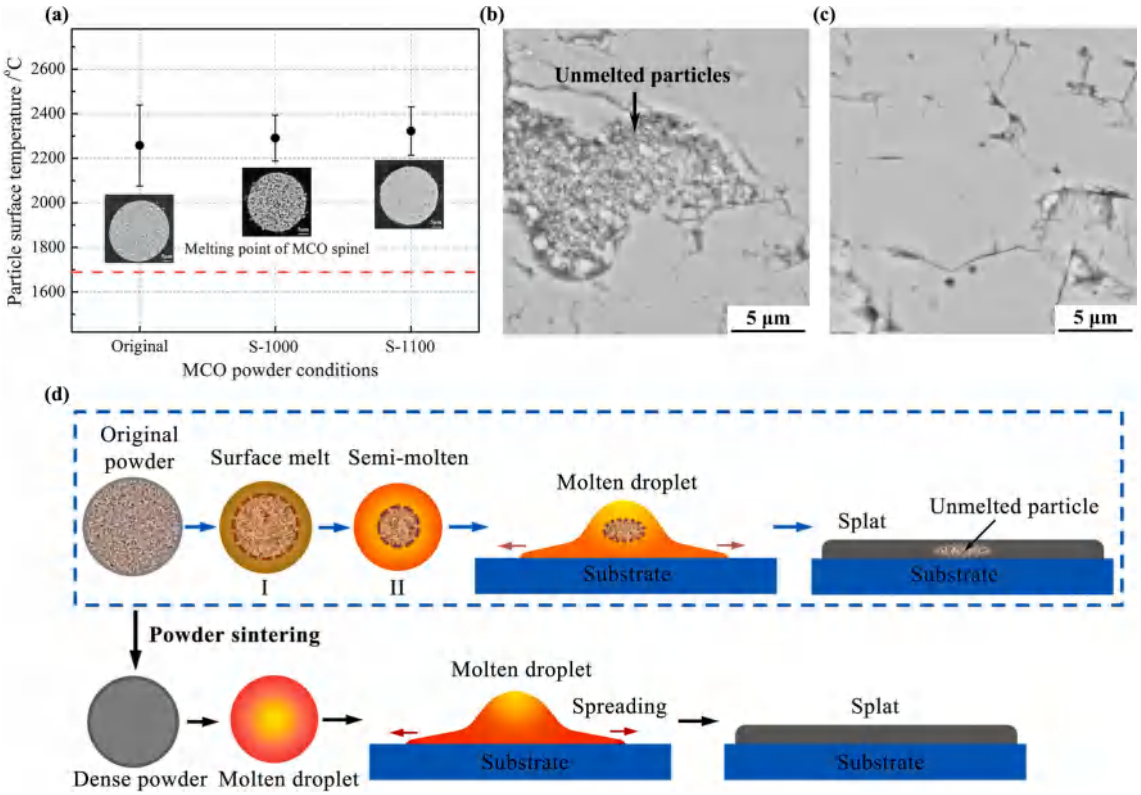

Fig. 3. (a) The inflight particle temperature for different MCO powder particles, MCO coatings deposited at room temperature by using: (b) original powders, (c) S-1100 sintering powders, and (d) the heating and deposition models of MCO particles during the coating deposition process. Note: S-1000 refers to MCO powders sintered at 1000 °C for 10 h, while S-1100 refers to 1100 °C for 2 h.

10–25 μm, METCO) were used as the feedstock for cathode, anode and electrolyte layer, respectively. Spherical FeCr24 powders with 24 wt% Cr (30–50 μm) and agglomerated $Mn_{1.5}Co_{1.5}O_4$ (MCO, 30–50 μm) powders acquired from Qingdao Tianyao Industrial co., LTD were used for the deposition of interconnector and protective layers.

Fig. 1 elaborates the manufacturing process of current thermally sprayed two-cell-stack assembled with MCO/FeCr24 interconnector. Firstly, a porous MgO-Al_2O_3 insulating layer in thickness of 120–150 μm was deposited onto the metal support, aiming at separating the single cells. Then all the cell components were prepared layer by layer onto the porous insulating layer through a commercial plasma spray system (GP-80, 80 kW class, China), in order of NiO/YSZ anode functional layer, YSZ electrolyte membrane, FeCr24/MCO interconnector and then $La_{0.8}Sr_{0.2}MnO_3$ (LSM) cathode. Four masks were utilized to deposit the abovementioned functional layers, the detailed technological parameters are listed in Table 1. To achieve dense structure with good interface bonding and high gas tightness, substrate preheating strategy was adopted for the fabrication of YSZ and MCO layers. Based on a self-assembly copper heating stage, the deposition temperature was maintained at a given value (550 °C, YSZ) and precisely monitored by an infrared pyrometer (RayRPM30L3U, Raytak, America) in the meanwhile. Then the protective Ar gas with a flow rate of 40 $L{\cdot}min^{-1}$ was supplemented through an argon gas shrouded attachment that was installed on the plasma torch, aiming to minimize the oxidation of inflight particles during the spraying process of FeCr24 interconnector. Afterwards, the half-cell was treated in H_2 atmosphere at 750 °C for 2 h, to ensure the sufficient reduction of NiO to Ni in the anode layers. At last, dense MCO protective coating was deposited at 400 °C, followed by the deposition of porous LSM cathode layer at room temperature (RT). The structural diagram of two-cell-stack assembled with MCO/FeCr24 interconnector is presented in Fig. 2(a).

2.2. Redox durability of MCO/FeCr24 interconnector

Prior to the performance test, the stability of thermally sprayed MCO/FeCr24 interconnector was investigated under both the 20 %H_2/Ar mixed gas atmosphere and H_2/Air redox conditions, in terms of phase, structural and electrical stabilities. First, the isothermal exposure was performed on MCO/FeCr24//MgO-Al_2O_3/SUS430 in dry 20 %H_2/Ar environment at 800 °C for 5 h, aiming to explore the microstructure feature of FeCr24 layers under reducing condition. While the second testing was carried out in a temperature range of 450–800 °C for 120 h, with MCO coating exposed in the flow of air atmosphere (cathode environment) and the SUS430 substrate exposed in H_2 flow at a rate of 0.3 slpm (anode environment), aiming to simulate the operation environment of tubular SOFCs. The detailed testing process can be found in previous work [53]. In addition, the electrical resistance of the interconnector was measured by four-point measurement simultaneously. Then the crystallographic phases for MCO coating at the top and bottom regions were respectively examined by X-ray diffraction (XRD) generator (RigakuD/Max-2400). The microstructures were characterized by scanning electron microscopy (SEM, MIRA 3 LMH, TESCAN, Czech Republic).

2.3. Performance of the segmented-in-series SOFC

The apparatus for output performance test is schematically shown in Fig. 2(c), where the two-cell-stack was first fixed onto one side of the quartz tubes by using Ag paste as the sealant, and then treated at 180 °C for 0.5 h to achieve the solidification of Ag sealant. The silver wires were subsequently attached onto the anode layer marked yellow in Cell #1 and cathode layer in Cell #2 by spot welding, aiming for current collection. During the performance testing, H_2 and Air with flow rate of 0.08 and 0.1 slpm were used as the fuel and oxidant gas, respectively. It's worth mentioning that the anode layer was exposed to H_2

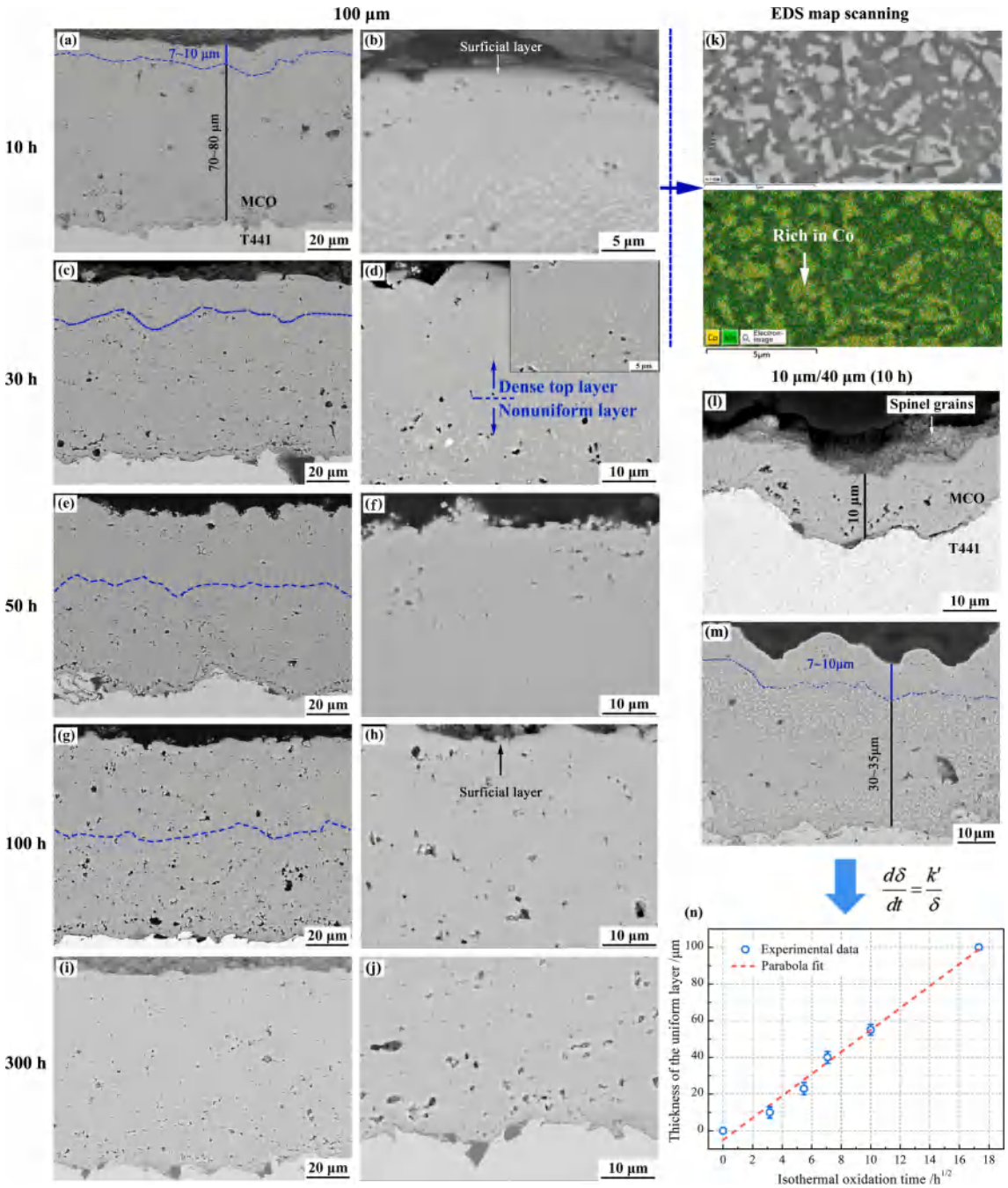

Fig. 4. The microstructure evolution of 100-μm-thick MCO coatings after exposure to air for: (a), (b) 10 h; (c), (d) 30 h; (e), (f) 50 h; (g), (h) 100 h; (i), (j) 300 h; (k) the corresponding EDS map scanning based on Figure (b); and (n) the growth dynamic curve; and SEM morphology for MCO coatings with thickness of (l) 10-μm and (m) 40-μm after exposure for 10 h; (n) homogenization rate for 100-μm MCO coatings. Note: δ denotes the thickness of upper uniform layer, t denotes the treatment durations; and k' denotes the oxidation rate constant.

atmosphere for reducing treatment (750 °C, 2 h) before the cell operation, in order to obtain uniform and porous Ni-YSZ composite anode structure. Then the output performance (I-V and I-P curves) of current two-cell-stack during several thermal cycling in temperature range of 600–800 °C was measured through the Keithley 2420 test station, while the electrochemical impedance spectra (EIS) under open circuit voltage (OCV) condition was characterized via the Solartron 1260/1287 electrochemical system. The test frequency range herein was set as 0.1–100 KHz, with an amplitude of alternating circuit (AC) voltage of 25 mV. In each thermal cycle, the cells in series were firstly operated at 600 °C, 650 °C, 700 °C and 750 °C for 15 min, respectively, and then held at 800 °C for 100 h to evaluate the output stability. All the above-mentioned tests were carried out in a tube furnace, with a heating/cooling rate of 3 °C·min^{-1}.

3. Results and discussions

3.1. Heating models for the molten MCO particles

In prior to the coating deposition, the inflight particle temperature for MCO powders under different states was monitored through particle diagnostic sensors (DPV-2000 from Saint-Bruno, QC, Canada). Fig. 3(a) presents the corresponding apparent temperatures for the inflight MCO particles under different states (original, S-1000, S-1100). Given the

same deposition parameters for MCO layer shown in Table 1, the average surface temperatures for different MCO powders is respectively 2257 °C, 2290 °C and 2321 °C, exhibiting a positive correlation trend with the powder density. The MCO coatings deposited at RT by using original agglomerated powders and S-1100 powders are presented in Fig. 3(b) and (c). Compared to the previous MCO coatings with pre-heating treatment at 400 °C [40], the coatings herein exhibit typical lamellar structure, characterized with non-bonding interfaces, micro-cracks and pores. Moreover, plenty of unmelted nanoparticles can be clearly observed in the coating prepared with original powders (see Fig. 3(b)), leading to an apparent porosity of 9.97 ± 0.83%. The apparent porosity herein was measured by using the image processing software "image J". As for each coating, the mean porosity was calculated from statistics on ten different regions. To prevent the coating from being damaged during the sample cutting process, the surface was first impregnated with E7-glue in vacuum, followed with drying treatment at 80 °C for 2 h.

Due to the high porosity, the original agglomerated MCO powders presented relatively low surface temperature and heat-transfer rate, leading to a semi-molten droplet with unmelted nanoparticles in the center. Then after impacting the substrates with high velocity, the semi-molten droplet spread out and solidified into a flattened particle with high porosity, see Fig. 3(d). In comparison, the sintered powders with high density exhibited improved surface temperature and heat-transfer rate, promoting the melting process for flying particles in the plasma jet flame. As a result, the fully molten droplet presented enhanced mobility and filling performance, contributing to flattened splat with lower porosity. This is further verified by the coating shown in Fig. 3(c), where no unmelted cluster was detected and lower apparent porosity (7.92 ± 0.66%) was obtained. After comprehensive consideration, sintered $Mn_{1.5}Co_{1.5}O_4$ powders (S-1100) with a particle range of 20–30 μm were utilized for the subsequent coating deposition.

3.2. Growth kinetics of the MCO spinel layers during post-annealing

When directly treated in air, inhomogeneous microstructure characterized with dense spinel top layer and non-uniform inner layer was detected for the APS-MCO coatings, leading to a reduced electrical property. This microstructure inhomogeneity was ascribed to the oxygen deficiency in the inner region, companied by the retarded diffusion of O/O_2 in the gradually densified top layer. So it is necessary to explore the evolution process (i.e. growth rate) of the top layer, which is critical to the structural uniformity and electrical properties of the whole spinel coating. In this study, MCO coatings with different thickness (10 μm, 40 μm, 100 μm) were exposed to isothermal oxidation at 800 °C for different durations (10 h, 30 h, 50 h, 100 h, 300 h), aiming to construct a quantitative characterization on the microstructure homogenization rate and determine a feasible coating thickness for the stack operation.

According to the microstructure evolution shown in Fig. 4, the coating thickness as well as the post-treatment durations exhibit remarkable effect on the coating homogeneity. When the coating is around 10 μm, a homogeneous spinel can be obtained after 10 h isothermal oxidation. While for coating in thickness of 40 and 100 μm, a distinct two-layer structure consisting of dense surficial layer (7–10 μm) and nonuniform inner layer is observed after testing for 10 h. EDS map scanning (see Fig. 4(k)) based on the inhomogeneous region characterized with light-colored precipitates and dark matrix indicates that the light region is in rich of Co, while the dark matrix is in rich of Mn. Nevertheless, the interface between the two layers gradually evolved towards the substrate side in prolonged oxidation process, see Fig. 4(a)–(j). As can be seen, the top layer gradually increases to 18–23 μm, 35–40 μm and then approximately 55–60 μm after testing for 30 h, 50 h and 100 h, respectively. When the duration prolongs to 300 h, a fully uniform microstructure is ultimately achieved. Based on the microstructure evolution of 100-μm-thick MCO coatings, a quantitative characterization on the microstructure homogenization rate ($d\delta/dt$) was established,

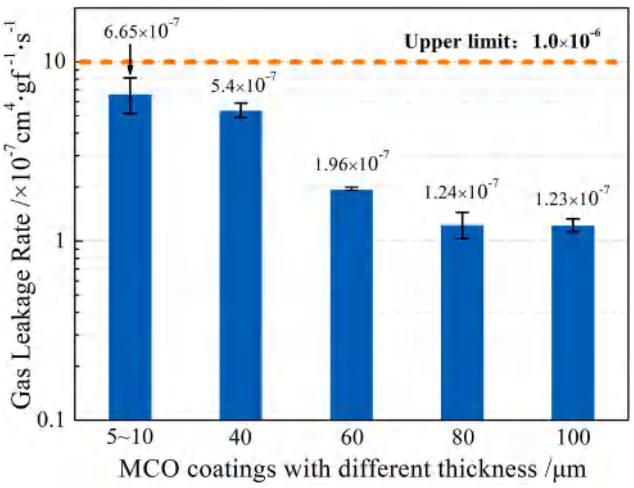

Fig. 5. The calculated gas leakage rate for as-sprayed MCO coatings with different thickness.

where δ denotes the thickness of upper uniform layer and t denotes the treatment duration. The statistics on δ-t values during isothermal oxidation illuminate the applicability of Wagner's theory [54–57] (Formula 1) for MCO spinel growth, where the thickness of uniform layers exhibits a parabolic relationship with the treatment duration, see Fig. 4(n). According to Formula 2, the homogenization rate ($d\delta/dt$) is inversely related to the thickness of upper uniform layer, which is opposed to the non-uniform area and only related to the treatment duration.

$$\delta^2 = 2k't \tag{1}$$

$$\frac{d\delta}{dt} = \frac{k'}{\delta} \tag{2}$$

Worth to mention is that the $d\delta/dt$ is also of inverse correlation with the coating thickness (δ_0), when the whole coating realizes fully homogenization (i.e. $\delta_0 = \delta$). As can be seen, the time required for fully homogenization is extended accordingly with the increasing of coating thickness, suggesting that a reasonable control for the thickness is necessary. However, the gas permeability for thermally sprayed ceramic coatings below 100 μm is usually inverse to the coating thickness. To achieve a high interface bonding strength, certain surface roughness is required for the substrates, which simultaneously lead to an uneven thickness and increased gas permeability especially for rather thin coating. Therefore, finding a balance between the thickness and uniformity is crucial for the coating application. Different from the apparent porosity, gas permeability herein is essentially based on the changes of differential pressure (ΔP) due to the gas leakage across the coatings, so can directly reflect the porosity of through pores. The testing apparatus and detailed calculations are supplemented in Fig. S2. To evaluate the influence of thickness (5–100 μm) on the density of as-sprayed MCO coatings, a comparison testing of the gas permeability was carried out. Based on the results shown in Fig. 5, the gas permeability for 10-μm-thick MCO coatings is 6.65 ± 0.49 × 10^{-7} $cm^4 \cdot gf^{-1} \cdot s^{-1}$, closed to the upper limit (10^{-6} order) for interconnect application. When it increased to about 60 μm, a further decreased value of 1.96 ± 0.04 × 10^{-7} $cm^4 \cdot gf^{-1} \cdot s^{-1}$ was obtained for the MCO coating. In spite of non-uniform chemical distribution in the initial stage, the deposited MCO layers with suitable thickness (i.e. 40–60 μm) could accomplish a uniform spinel structure after post-annealing or operation under oxidizing environment for less than 100 hrs, indicating the feasibility for stack operations.

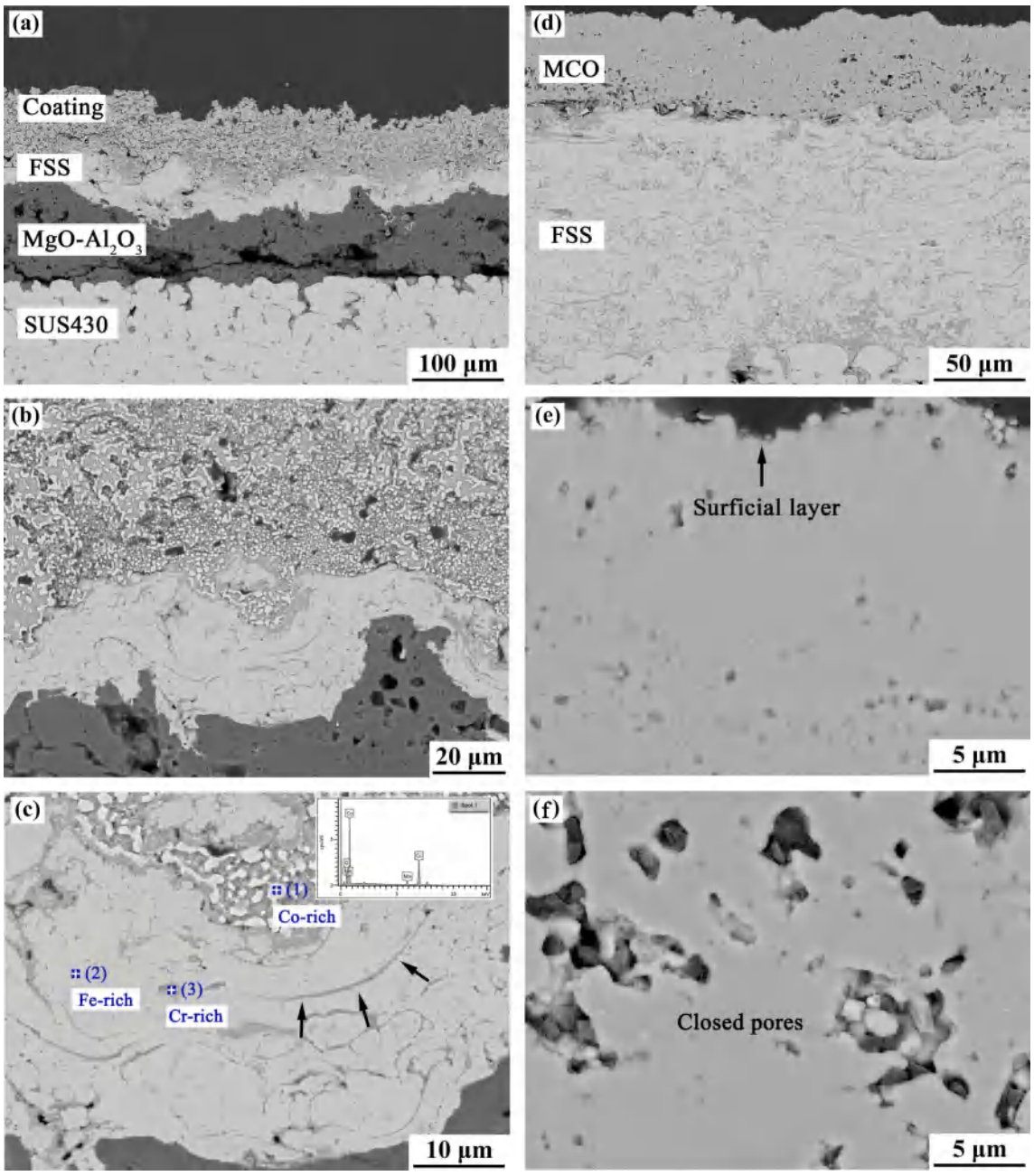

Fig. 6. (a)-(c) SEM and EDS data for MCO/FeCr24 interconnector after exposed in 20 %H_2/Ar atmosphere at 800 °C for 5 h; and the morphology for MCO/FeCr24 interconnector after testing in H_2/Air redox atmosphere at 800 °C for 120 h: (d) MCO/ FSS, (e) the upper, and (f) bottom region of MCO coating.

3.3. Redox stability of the MCO/FeCr24 interconnector

Based on the specific structure of our tubular segmented-in-series SOFCs shown in Fig. 2(a), the interconnector deposited onto MgO-Al_2O_3/SUS430 support is exposed to both anode and cathode environments simultaneously. The metal part would suffer from oxidation, while the oxide part would suffer from reduction. Therefore, the stability of interconnector under both reducing and oxidizing conditions is vital to the real stack operation. According to previous work, the $MnCo_2O_4$ coatings exposed to H_2/Air redox atmosphere presented a bilayer structure consisting of relatively dense upper layer (spinel) and porous bottom layer (MnO/Co), revealing the partial decomposition of $MnCo_2O_4$ spinel [53]. So it is necessary to develop a composite interconnector for the tubular SOFCs, considering the instability of single spinel coating under redox condition. In this work, the stability of thermally sprayed MCO/FeCr24 interconnector have been investigated under both the 20 %H_2/Ar mixed gas atmosphere and H_2/Air redox atmospheres, in terms of phase, structural and electrical stabilities. The testing performed on MCO/FeCr24 interconnector//MgO-Al_2O_3 insulating layer//SUS430 support under H_2/Ar mixed gas atmosphere is designed to explore the microstructure feature of thermally sprayed FeCr24 layers under single reducing condition. The introduction of Ar aims at adjusting the oxygen pressure and meanwhile slowing down the reaction process. While the subsequent testing carried out under H_2/Air reducing-oxidizing (redox) atmospheres aims to further evaluate the structural and electrical performance under simulating conditions of tubular SOFCs.

According to the cross-sectional morphology shown in Fig. 6(a) and (b), the MCO coatings exposed to H_2/Ar mixed gas atmosphere appear to be rather porous, while the interconnector layer exhibits high gas-

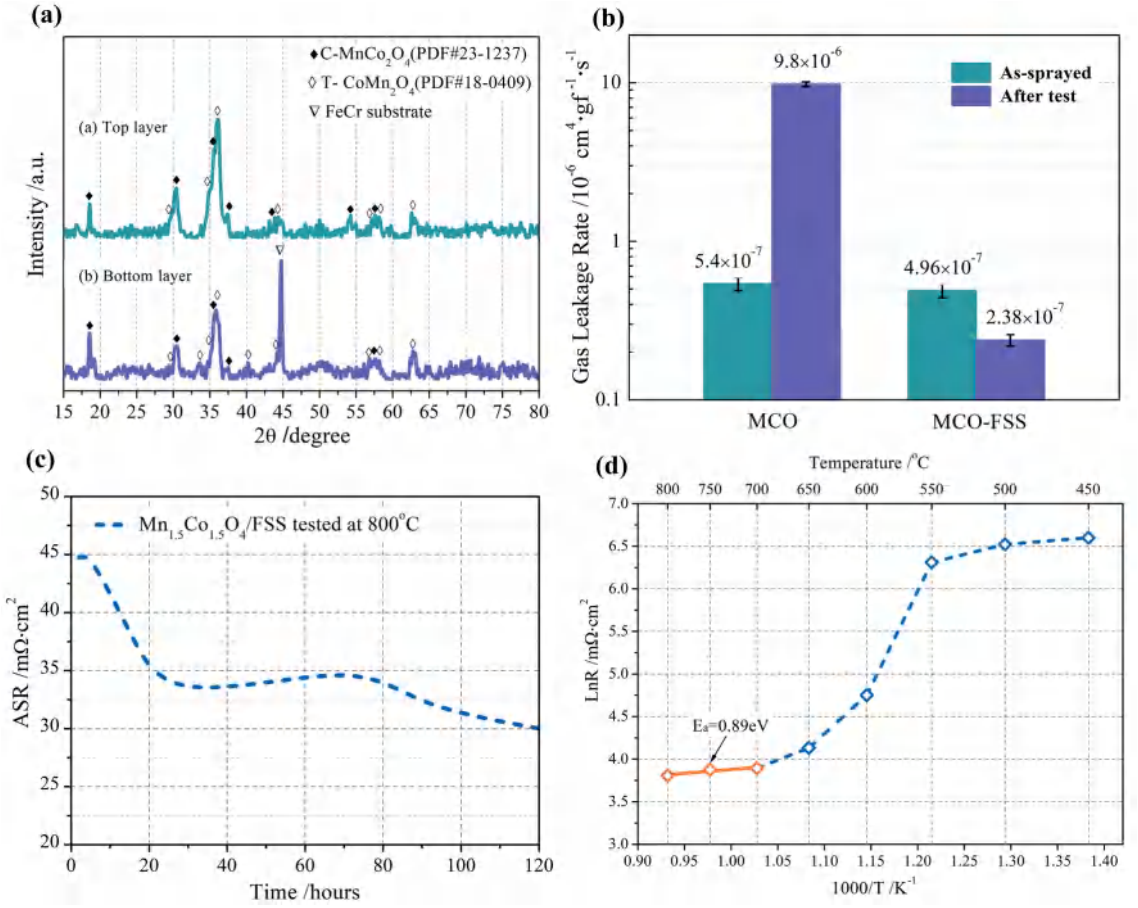

Fig. 7. (a) XRD analysis on the MCO/FeCr24 interconnector after 120 h test under redox atmosphere; (b) gas leakage rate of the MCO coatings and MCO/FeCr24 interconnector at different stages; (c) ASR value for the MCO/FeCr24 interconnector under redox condition at 800 °C; and (d) Arrhenius plots at different temperatures.

tightness. Based on the dot scanning shown in Fig. 6(c), the light particles marked as spot 1 is in rich of Co (with a Co/Mn ration of 47.08/2.92), which was induced by the fully decomposition of MCO spinel and further demonstrates the instability of spinel coating under low-$p(O_2)$ environment. As for FeCr24 layers, the light and dark region marked as spot 2,3 is respectively in rich of Fe (with a Fe/Cr ration of 85.9/14.1) and Cr (with a Fe/Cr ration of 22.7/77.3), while the grey strip region marked by arrows is comprised of Cr_2O_3. The H_2 used in the redox stability test has a gas purity of 99.99%, with a maxmium volume concentration of 5 ppm for O_2 and 10 ppm for H_2O, while the Ar gas with the same purity also contains 10 ppm of O_2 and 15 ppm of H_2O. Based on the Dalton's law of partial pressure, the 20 %H_2/Ar mixed gas herein presents a low oxygen pressure ($p(O_2)$) of 1.65×10^{-3} atm, but is still well above the critical value of Cr_2O_3 (3.8×10^{-28} atm, 800 °C). This also explains the existence of Cr_2O_3 scales detected in the FeCr24 coatings. However, different morphology was obtained for the MCO coating, which is characterized with high density in the upper region and unconnected micro-pores in the bottom region after exposure to H_2/Air redox atmosphere for 120 h. Moreover, the MCO coating exhibits a good adhesion with FSS interconnector and no crack is detected after testing, see Fig. 6(d)–(f). This structural character is similar with the MCO/bulk T441 as treated in oxidizing environment, illustrating the effectivity of thermally sprayed FeCr24 coatings. On condition that the FeCr24 matrix could effectively block the in-diffusion of H/H_2, the operating conditions could be more closed to that of planar cells.

Afterwards, XRD was respectively performed on the top region (exposed to oxidizing atmosphere) and bottom region (near to the FSS interconnector) for the MCO coatings exposed to H_2/Air redox atmosphere. After XRD analysis on the top layer, MCO coating with a depth of approximately 40 μm was removed from the surface side through careful polishing, and then x-ray diffraction was performed on the bottom layer in thickness of 10 μm. As indicated in Fig. 7(a), the coating is still comprised of cubic $MnCo_2O_4$ and tetragonal $CoMn_2O_4$ spinel phases, demonstrating that the thermally sprayed MCO/FeCr24 interconnector has excellent microstructure stability under the redox condition. Meanwhile, the FeCr24 layer could effectively prevent the above MCO coating from anodic reduction atmosphere. The strong diffraction peak detected at 44.7° corresponds to the Fe-Cr matrix, since the X-ray with an investigation depth of about ten several micrometers could penetrate the bottom layer. Given the rigorous operation environment, gas permeability of the interconnector should be below the critical value (10^{-6} $cm^4 \cdot gf^{-1} \cdot s^{-1}$). The rather low value of 2.38×10^{-7} $cm^4 \cdot gf^{-1} \cdot s^{-1}$ (see Fig. 7(b)) for the tested MCO/FeCr24 interconnector indicated a high density, which can be ascribed to the densification of both the MCO and FSS interconnectors. The surface energy minimization leads to the coalescence of small isolated pores in middle and bottom regions, accompanied by the densification of the free top layer during the sintering process for MCO coating. On the other side, the Cr-rich oxidation layers filled in the non-bonded interface for the APS-FeCr24 coating further enabled the interconnector with improved density.

At last, the interfacial ASR was measured as a function of time in H_2/Air environment at 800 °C for 120 h, aiming to evaluate the electrical performance of the thermally sprayed MCO/FeCr24 interconnector under redox condition in tubular SOFC stacks. Fig. 7(c) demonstrates the resistance variation with the duration time, which can be divided into

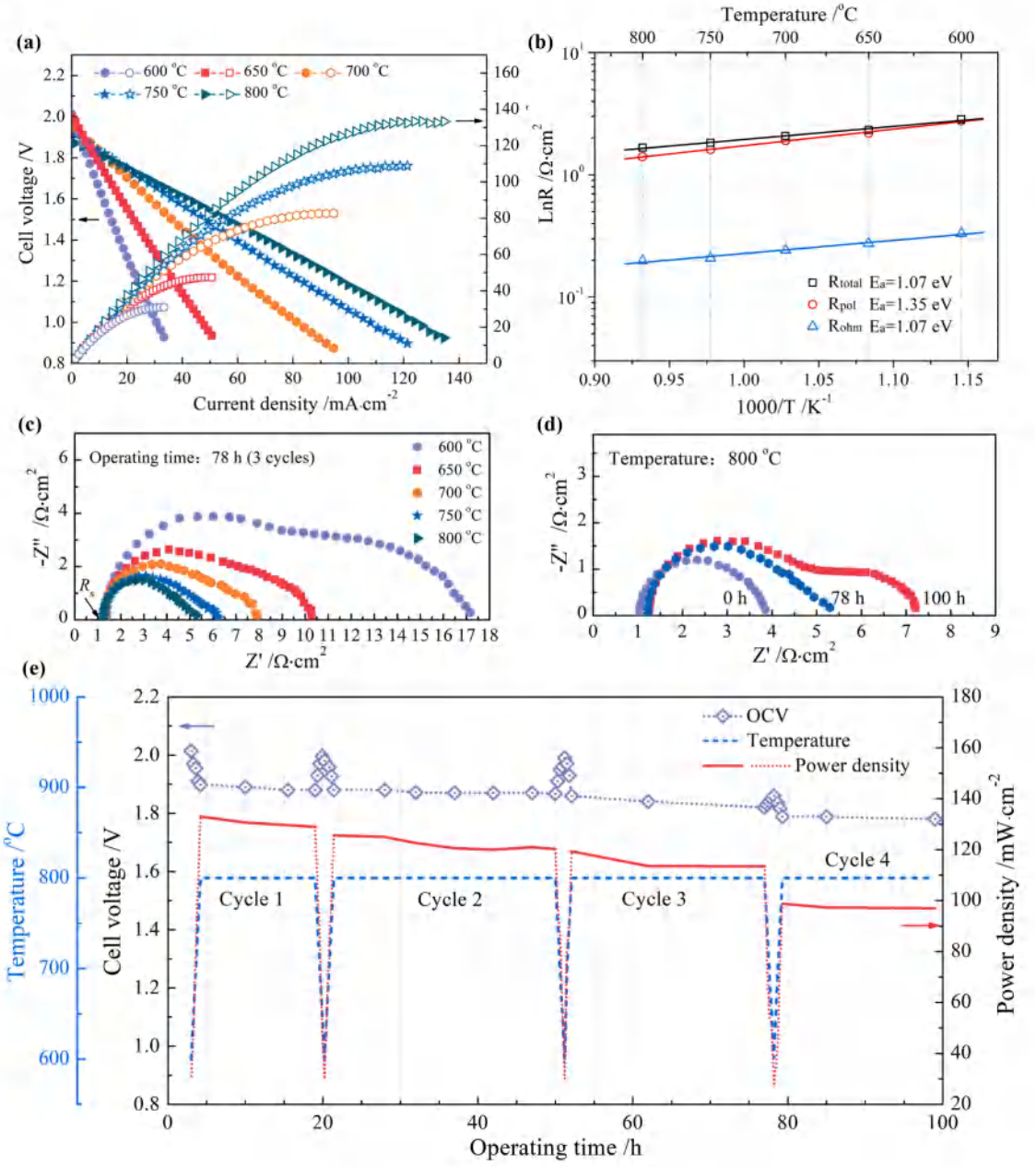

Fig. 8. Output performance of current two-cell-stack assembled with MCO/FeCr24 interconnector: (a) I-V curves; (b) Arrhenius plots at different temperatures; and electrochemical impedance spectra (c) at different temperatures, (d) at 800 °C for different thermal cycles; (e) the thermal cycling stability.

two stages: (i) a rapid descent stage in the initial 20-h, and (ii) a steady decline stage in the later 100-h. The significant drop from the initial 45 $m\Omega \cdot cm^{-2}$ to 35 $m\Omega \cdot cm^{-2}$ observed in the first 20-h is mainly attributed to two factors: (a) the reformation and homogenization of spinel structure in the first few hundreds of hours, as discussed before, and (b) the enhanced interfacial adhesion between each part. At the end of 120-h test cycle, the resistance further decreased to 30 $m\Omega \cdot cm^2$, still a little higher than the previous reported MCO/bulk T441 (23 $m\Omega \cdot cm^2$) [40]. The observed ASR is attributed to three parts: (i) the MCO protective coating, (ii) the FSS interconnector, and (iii) the SUS430 substrate. $Mn_{1.5}Co_{1.5}O_4$ exhibits a gradually enhanced conductivity with the increasing temperature, which varies from 5 $S \cdot cm^{-1}$ (T = 500 °C) to 100 $S \cdot cm^{-1}$ (T = 900 °C) under the air atmosphere.[50] In addition, the electrical conductivity of bulk FSS and SUS430 could reach a magnitude of 10^3 $S \cdot cm^{-1}$ in range of 450–800 °C, considerably higher than MCO and Cr-rich oxide scales (0.006–0.02 $S \cdot cm^{-1}$, 700–800 °C). Therefore, the relatively higher resistance herein was mainly ascribed to the Cr_2O_3, considering the massively distributed Cr-rich oxide scales in the thermally sprayed FSS layers. As shown in Fig. 7(d), the resistance (LnR) of MCO coating exhibits a nonlinear distribution trend in the temperature (1/T) range of 450–800 °C. Nevertheless, a linear relationship can still be observed in range of 700–800 °C. The calculation based on the Arrhenius equation indicated an activation energy (E_A) of 0.89 eV for the thermally sprayed MCO/FeCr24 interconnector under the redox atmosphere at 700–800 °C, which is closed to that of bulk $Mn_{1.5}Co_{1.5}O_4$ (0.6 eV). To facilitate the SOFC stacks with a higher output performance, the interconnector should have an electrical conductivity above 1 $S \cdot cm^{-1}$. [58] The shortest transport path for the electrons in this work is approximately 0.14 cm, and the resultant conductivity of the MCO/FeCr24 interconnector is about 3.1–4.7 $S \cdot cm^{-1}$, which could meet the requirement for tubular SOFC stacks.

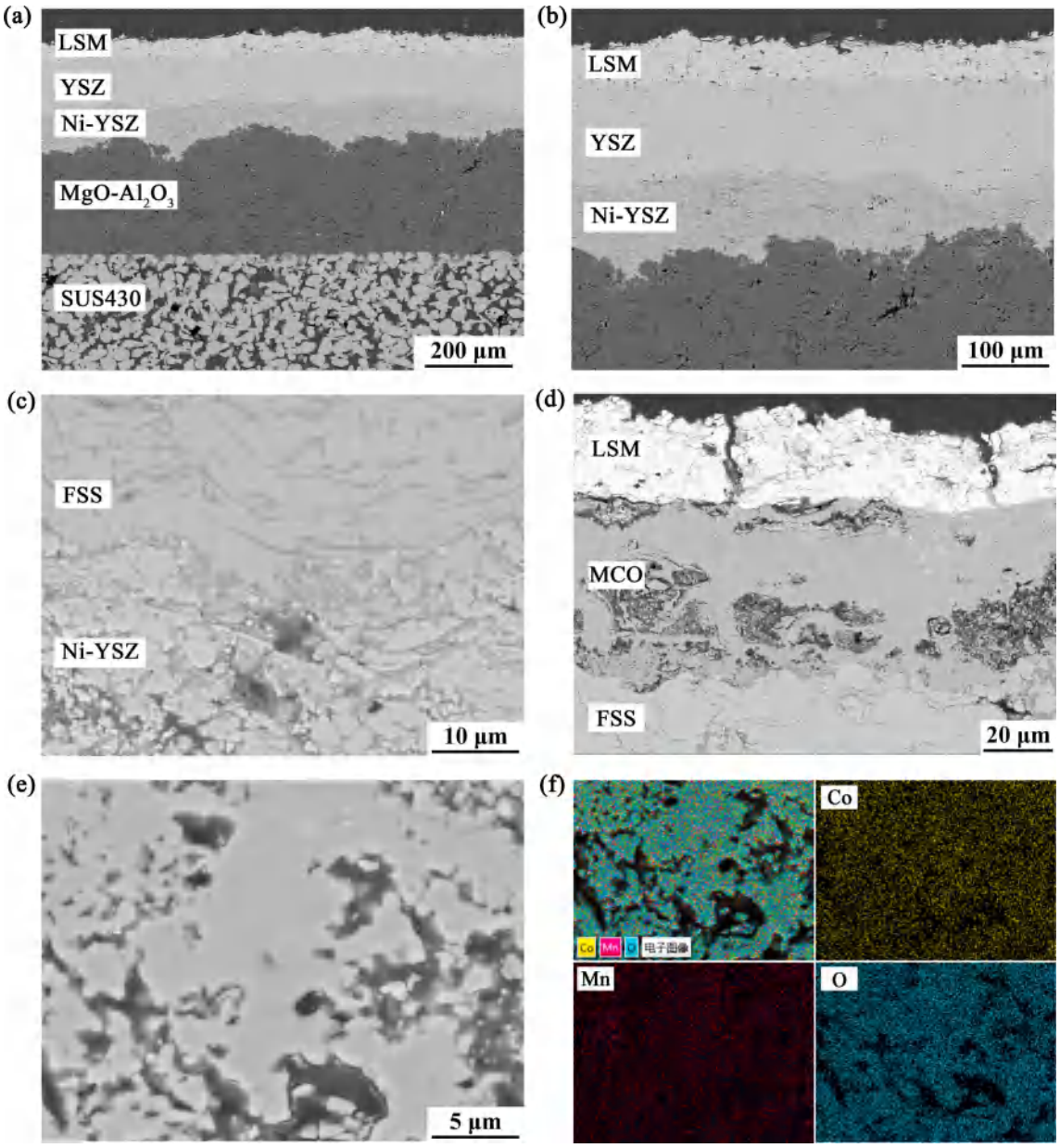

Fig. 9. Cross-sectional morphology of the tested cells: (a), (b) the single cell; (c) the interconnector/anode; (d) the cathode/interconnector; (e) the structure and (f) EDS map scanning based on MCO coating.

3.4. Output performance of the two-cell-stack during several thermal cycles

Considering the relatively low cost and simple preparing process, segmented-in-series SOFCs based on sheet SUS430 support were finally assembled through APS process, and then exposed to real operating environment of tubular SOFCs. The density of APS ceramic coatings is inversely proportional to the thickness, especially for coatings less than 100 μm.[59] According to Tsukudaet al., the stacks based on low pressure plasma sprayed (LPPS) electrolyte layer with thickness of 100 μm delivered a V_{OC} of 1 V at 1000 °C for each single cell.[60] Malzbender et al. introduced an APS-$MnCo_{1.9}Fe_{0.1}O_4$ protective coating for Crofer22 APU interconnect, and obtained a maximum V_{OC} of 1.05 V for the planar stack at 840 °C [61]. Based on a 50–60 μm dense YSZ electrolyte prepared through high speed plasma spraying (SAPS) process, the single cell developed by Zhang et al. delivered a maximum V_{OC} of 1.02 V at 600–800 °C. The resultant tubular SOFCs consisting of 6 cells (LSM/YSZ/Ni-YSZ) in series were then produced through APS process, and delivered a maximum output power of 117 mW·cm^{-2} at 800 °C [15]. In current work, an average open circuit voltage (V_{OC}) up to 1 V is achieved for the single cells at 600 °C (see Fig. 8(a)), suggesting that the density of YSZ and MCO/ FeCr24 interconnector layers deposited via APS process had already meet the requirements for SOFCs. Moreover, the resultant two-cell-stack based on MCO/FeCr24 interconnector delivered a max output power density of 133 mW·cm^{-2} at 800 °C, with an average voltage degradation of less than 1.8%·cycle^{-1} after 3 thermal cycles from 600 °C to 800 °C for 78 h, as shown in Fig. 8(e). Unfortunately, significant drop in both the voltage and power density was detected after the 4th cycling. The stack performance is determined by both the output voltage and the internal resistance. With increasing of the operation temperature, the V_{OC} gradually decreases and then the internal resistance variation plays a decisive role in the stack performance.

Fig. 8(c) and (d) indicate the typical impedance spectra for cells tested at different temperatures, and after different thermal cycles at 800 °C, respectively. The polarization resistance (Z_{pol}) includes contributions from both the anode and the cathode, and can be estimated from

Table 2
TEC values of each electrode in current thermally sprayed stack ($\times 10^{-6}\cdot K^{-1}$, 600–800 °C).

SOFC components	SUS430 support tube	Ni/8YSZ	8YSZ	FeCr24	MCO	LSM
TEC value	12.6–12.8	~11.5	10.5	12.3–12.5	12.77	11.08

the diameter of the impedance loops. Whereas the ohmic resistance (R_{ohm}) is primarily attributed to the resistance of electrolyte (R_{elyt}) and interconnector ($R_{connect}$), which can be determined from the intercepts with the abscissa at high frequencies of the impedance spectra. Worth to mentioned is that the R_{elyt} was basically constant within the test cycles, so the R_{ohm} was dominated mainly by the interconnector layers. Since the resistance for single cells was primarily contributed by YSZ electrolyte, which has a much lower ionic conductivity (0.03 $S\cdot cm^{-1}$ at 800 °C) than the LSM (180 $S\cdot cm^{-1}$) and Ni-YSZ (> 1000 $S\cdot cm^{-1}$) electrodes. Whereas for the cells in series, the interconnector plays a critical role in the device resistance. The previous reported single cells constructed with thermally sprayed LSM/YSZ/Ni-YSZ exhibited an impedance of 0.85 $\Omega\cdot cm^2$, indicating that the R_{ohm} for the cells in series should be above 0.85 $\Omega\cdot cm^2$. Based on the initial R_{ohm} of 1.03 $\Omega\cdot cm^2$ shown in Fig. 8(d), we can calculate that the initial $R_{connect}$ was closed to 0.18 $\Omega\cdot cm^2$, which increased by about 0.22 $\Omega\cdot cm^2$ after 4 thermal cycles lasting for 100 hrs. Moreover, the enhanced resistance was mainly ascribed to the MCO protective coating, since the conductivity of MCO (10–68 $S\cdot cm^{-1}$)[50] is much lower than FSS (5000–4000 $S\cdot cm^{-1}$) during the temperature range of 600–800 °C. In our current segmented-in-series SOFC stacks, the interconnector layer indicates a more complicated resistance change and the interface resistance cannot be evaluated properly, since it overlaps with both the cathode and anode, and does not have a regular geometry. On the other hand, the initial Z_{pol} in this study is 2.82 $\Omega\cdot cm^2$, closed to the reported 2 $\Omega\cdot cm^2$ for LSM/YSZ at 800 °C, indicating that the activation polarization is mainly attributed to the electrodes. As shown in Fig. 8(b), the resistance (Ln R) showed a good linear relationship with the temperature (1/T). Based on the Arrhenius equation, the activation energy corresponding to the ohmic and activation polarizations is respectively 1.07 eV and 1.35 eV. In the anode supported cell constructed with Ni-YSZ/YSZ/Ni-YSZ, the electrolyte and anode both exhibited an E_A of 0.8 eV, while the LSM cathode had a much higher value of 1.4–2 eV, closed to the value in this work.

To reveal the increased polarization resistance and subsequent performance degradation, post-test analysis on the microstructure was carried out for the cells in series. As shown in Fig. 9(a) and (b), the two single cells, in combination with the dense interconnector both exhibit good interface bonding, which contributes to a decreased contact resistance and ohmic resistance. Besides, the upper region with thickness of above 20 μm exhibits a relatively high density for the MCO coating, while an increased porosity is observed in the bottom region (Fig. 9(d)). EDS test performed on the porous bottom region indicates a homogeneous microstructure with atomic ratio of 50.3Mn/49.7Co, which is closed to the initial MCO coating. Here we can conclude that the FeCr24 interconnector has effectively prevented the reducing atmosphere from the anode side, and enables the MCO coating with enhanced stability to some degree during the thermal cycles. The performance degradation during the thermal cycling is mainly attributed to the failed cathode layers, where large longitudinal cracks are detected in the part contact with the interconnector layers. The present observations indicate that cathode failure herein is likely due to a combination of various phenomena: tensile stress from slight thermal mismatching, and then stress concentration in the overlapping area of LSM/MCO. It is well known that the typical Ni-8YSZ/8YSZ/LSM combinations are thermo-mechanically compatible with each other, which is also verified by the intact structure of single cell part (Fig. 9a and b). According to the thermal expansion coefficients (TECs) of each functional layer listed in Table 2, the prepared electrolyte and electrodes have closed TECs, slightly lower than the interconnector layers. This discrepancy in thermal expansion is highly possible to subject the cathode layer to tensile stress during stack heating. Combined with the stress concentration, this outermost overlap region between the cathode/interconnector layers (Fig. 2a) has a much higher cracking tendency during multiple thermal cycles. Under tensile conditions, through-thickness cracks are likely to develop from pre-existing defects (i.e. pore, microcrack) in the thermally sprayed LSM layer and eventually lead to the stack degradation. To optimize the thermal matching between the LSM/MCO layers and reduce the cracking tendency, composite interconnector can be considered by introducing a $(La,Sr)TiO_3$ outer layer with suitable TEC of ~11 × $10^{-6}\cdot K^{-1}$ into the interconnector.

4. Conclusions

In summary, the MCO/FeCr24 interconnector layers prepared via

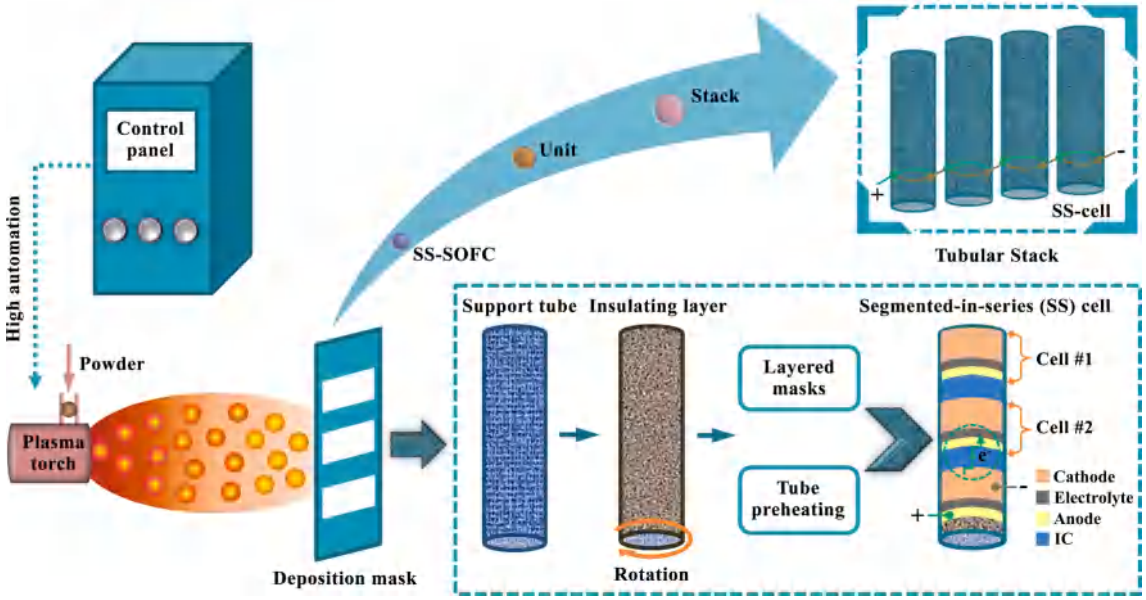

Fig. 10. Schematic diagram for the large-scale assembling of thermally sprayed tubular SOFC stacks.

APS technique have achieved a high redox durability under the tubular stack environment, indicating a promising application prospect. Worth to mentioned is that the planar circular cell in this work is actually a partial reflection of our tubular segmented-in-series SOFC, indicated as the green circular region in Fig. 10. Herein the manufacturing process was simplified and other related factors were minimized, since current work is focused on the feasibility of thermally-sprayed FeCr24/MCO interconnector layers rather than the tubular stacks. It was demonstrated that densified MCO powder particles contribute to improved surface temperature and melting degree, as well as enhanced coating density. It was also confirmed that the homogenization rate ($d\delta/dt$) for MCO coatings under oxidizing atmosphere is inversely related to the coating thickness (δ_0), which suggests an appropriate thickness of ~60 μm for subsequent SOFC applications. Besides, the thermally sprayed MCO/FeCr24 interconnector exhibited stable phase structure, low gas permeability of 2.38 × 10^{-7} $cm^4 \cdot gf^{-1} \cdot s^{-1}$ and adequate electrical conductivity of 4.7 $S \cdot cm^{-1}$ under H_2/Air redox atmosphere at 800 °C, indicating a promising feasibility for tubular SOFC applications. The resultant segmented-in-series stacks based on this MCO/FeCr24 interconnector delivered a max output power density of 133 $mW \cdot cm^{-2}$ at 800 °C, with an average voltage degradation of less than 1.8%·$cycle^{-1}$ after 3 thermal cycles from 600 °C to 800 °C for 78 h. The FeCr24 interconnector has effectively prevented the reducing atmosphere from the anode side, and enables the MCO coating with enhanced stability to some degree during the thermal cycles. Unfortunately, the discrepancy in thermal expansion subjects the cathode layer to tensile stress, leading to crack growth, dramatically increased polarization resistance and then degraded device performance. To address this issue, future efforts should be taken in constructing composite interconnector layers to optimize the thermal matching between the cathode/interconnector layers.

CRediT authorship contribution statement

Yingzhen Hu: Data curation, Writing – original draft. **Jiu-Tao Gao:** Methodology, Investigation. **Cheng-Xin Li:** Supervision. **Chang-Jiu Li:** .

Declaration of Competing Interest

The authors declare that they have no known competing financial interests or personal relationships that could have appeared to influence the work reported in this paper.

Acknowledgements

This work was financially supported by the National Natural Science Foundation of China (Grant 51901187), the General Special Scientific Research Program of Education Department of Shaanxi Provincial (Grant 21JK0725), and the Natural Science Basic Research Program of Shaanxi (Grant 2019JQ-612). We declare no competing financial interests.

Appendix A. Supplementary material

Supplementary data to this article can be found online at https://doi.org/10.1016/j.apsusc.2022.152861.

References

[1] Z. Liu, M. Chen, M. Zhou, D. Cao, P. Liu, W. Wang, M. Liu, J. Huang, J. Shao, J. Liu, Multiple effects of iron and nickel additives on the properties of proton conducting yttrium-doped barium cerate-zirconate electrolytes for high-performance solid oxide fuel cells, ACS Appl. Mater. Interfaces 12 (2020) 50433–50445.
[2] Q. Qiu, M. Zhou, W. Cai, Q. Zhou, Y. Zhang, W. Wang, M. Liu, J. Liu, A comparative investigation on direct carbon solid oxide fuel cells operated with fuels of biochar derived from wheat straw, corncob, and bagasse, Biomass Bioenergy 121 (2019) 56–63.
[3] X. Chen, W. Ni, X. Du, Z. Sun, T. Zhu, Q. Zhong, M. Han, Electrochemical property of multi-layer anode supported solid oxide fuel cell fabricated through sequential tape-casting and co-firing, J. Mater. Sci. Technol. 35 (2019) 695–701.
[4] H.B. Li, N. Xu, Y.H. Fang, H. Fan, Z. Lei, M.F. Han, Syngas production via coal char-CO_2 fluidized bed gasification and the effect on the performance of LSCFN//LSGM//LSCFN solid oxide fuel cell, J. Mater. Sci. Technol. 34 (2018) 403–408.
[5] W. Kong, W. Zhang, H. Huang, Y. Zhang, J. Wu, Y. Xu, Analysis of micro-tubular SOFC stability under ambient and operating temperatures, J. Mater. Sci. Technol. 34 (2018) 1436–1440.
[6] J. Ding, J. Liu, A novel design and performance of cone-shaped tubular anode-supported segmented-in-series solid oxide fuel cell stack, J. Power Sources 193 (2) (2009) 769–773.
[7] M. Suzuki, S. Inoue, T. Shigehisa, Field test result of residential SOFC CHP system over 10 Years, 89000 Hours, ECS Trans. 103 (1) (2021) 25–30.
[8] J. Otomo, J. Oishi, K. Miyazaki, S. Okamura, K. Yamada, Coupled analysis of performance and costs of segmented-in-series tubular solid oxide fuel cell for combined cycle system, Int. J. Hydrogen Energy 42 (30) (2017) 19190–19203.
[9] K. Fujita, T. Somekawa, K. Horiuchi, Y. Matsuzaki, Evaluation of the redox stability of segmented-in-series solid oxide fuel cell stacks, J. Power Sources 193 (1) (2009) 130–135.
[10] K. Okumura, Y. Aihara, S. Ito, S. Kawasaki, Development of thermal spraying-sintering technology for solid oxide fuel cells, J. Therm. Spray Technol. 9 (2000) 354–359.
[11] H. Tsukuda, A. Notomi, N. Hisatome, Application of plasma spraying to tubular-type solid oxide fuel cells production, J. Therm. Spray Technol. 9 (2000) 364–368.
[12] Y. Kobayashi, Y. Ando, M. Nishiura, H. Kishizawa, M. Iwata, N. Matake, K. Tomida, Recent progress of SOFC combined cycle system with segmented-in-series tubular type cell stack at MHI, ECS Trans. 57 (1) (2013) 53–60.
[13] J.-T. Gao, J.-H. Li, Y.-P. Wang, C.-J. Li, C.-X. Li, Performance and stability of plasma-sprayed 10 × 10 cm^2 self-sealing metal-supported solid oxide fuel cells, J. Therm. Spray Technol. 30 (4) (2021) 1059–1068.
[14] S.-H. Liu, J.P. Trelles, A.B. Murphy, W.-T. He, J. Shi, S. Li, C.-J. Li, C.-X. Li, H.-B. Guo, Low-pressure plasma-induced physical vapor deposition of advanced thermal barrier coatings: microstructures, modelling and mechanisms, Mater. Today Phys. 21 (2021) 100481, https://doi.org/10.1016/j.mtphys.2021.100481.
[15] S.-L. Zhang, C.-X. Li, S. Liu, C.-J. Li, G.-J. Yang, P.-J. He, L.-L. Yun, B.o. Song, Y.-X. Xie, Thermally sprayed large tubular solid oxide fuel cells and its stack: geometry optimization, preparation, and performance, J. Therm. Spray Technol. 26 (3) (2017) 441–455.
[16] I. Antepara, I. Villarreal, L.M. Rodríguez-Martínez, N. Lecanda, U. Castro, A. Laresgoiti, Evaluation of ferritic steels for use as interconnects and porous metal supports in IT-SOFCs, J. Power Sources 151 (2005) 103–107.
[17] J. Froitzheim, G.H. Meier, L. Niewolak, P.J. Ennis, H. Hattendorf, L. Singheiser, W. J. Quadakkers, Development of high strength ferritic steel for interconnect application in SOFCs, J. Power Sources 178 (2008) 163–173.
[18] H. Abdoli, S. Molin, H. Farnoush, Effect of interconnect coating procedure on solid oxide fuel cell performance, Mater. Lett. 259 (2020) 126898.
[19] M. Park, J.S. Shin, S. Lee, H.J. Kim, H. An, H.i. Ji, H. Kim, J.W. Son, J.H. Lee, B.K. Kim, H.W. Lee, K.J. Yoon, Thermal degradation mechanism of ferritic alloy (Crofer 22 APU), Corros. Sci. 134 (2018) 17–22.
[20] R. Wang, Z. Sun, U.B. Pal, S. Gopalan, S.N. Basu, Mitigation of chromium poisoning of cathodes in solid oxide fuel cells employing $CuMn_{1.8}O_4$ spinel coating on metallic interconnect, J. Power Sources 376 (2018) 100–110.
[21] B. Talic, V. Venkatachalam, P.V. Hendriksen, R. Kiebach, Comparison of $MnCo_2O_4$ coated Crofer 22 H, 441, 430 as interconnects for intermediate-temperature solid oxide fuel cell stacks, J. Alloy. Compd. 821 (2020) 153229.
[22] Y.Z. Hu, L.L. Yun, T. Wei, C.X. Li, Z. Qi, G.J. Yang, C.J. Li, M. Liu, Aerosol sprayed $Mn_{1.5}Co_{1.5}O_4$ protective coatings for metallic interconnect of solid oxide fuel cells, Int. J. Hydrogen Energy (2016).
[23] M.R. Ardigo-Besnard, I. Popa, S. Chevalier, Effect of spinel and perovskite coatings on the long term oxidation of a ferritic stainless steel in H_2/H_2O atmosphere, Corros. Sci. 148 (2019) 251–263.
[24] J.G. Grolig, J. Froitzheim, J.-E. Svensson, Coated stainless steel 441 as interconnect material for solid oxide fuel cells: evolution of electrical properties, J. Power Sources 284 (2015) 321–327.
[25] C. Jia, Y. Wang, S. Molin, Y. Zhang, M. Chen, M. Han, High temperature oxidation behavior of SUS430 SOFC interconnects with Mn-Co spinel coating in air, J. Alloy. Compd. 787 (2019) 1327–1335.
[26] A. Mosavi, H. Ebrahimifar, Investigation of oxidation and electrical behavior of AISI 430 steel coated with Mn-Co-CeO_2 composite, Int. J. Hydrogen Energy 45 (2020) 3145–3162.
[27] W.N. Liu, X. Sun, E. Stephens, M.A. Khaleel, Life prediction of coated and uncoated metallic interconnect for solid oxide fuel cell applications, J. Power Sources 189 (2009) 1044–1050.
[28] Y. Zhang, A. Javed, M. Zhou, S. Liang, P. Xiao, Fabrication of Mn-Co spinel coatings on crofer 22 APU stainless steel by electrophoretic deposition for interconnect applications in solid oxide fuel cells, Int. J. Appl. Ceram. Technol. 11 (2014) 332–341.
[29] R. Wang, M. Würth, U.B. Pal, S. Gopalan, S.N. Basu, Roles of humidity and cathodic current in chromium poisoning of Sr-doped $LaMnO_3$-based cathodes in solid oxide fuel cells, J. Power Sources 360 (2017) 87–97.
[30] L. Zhou, J.H. Mason, W. Li, X. Liu, Comprehensive review of chromium deposition and poisoning of solid oxide fuel cells (SOFCs) cathode materials, Renew. Sustain. Energy Rev. 134 (2020) 110320.
[31] M. Stanislowski, E. Wessel, K. Hilpert, T. Markus, L. Singheiser, Chromium vaporization from high-temperature alloys: I. Chromia-forming steels and the

influence of outer oxide layers, J. Electrochem. Soc. 154 (4) (2007) A295, https://doi.org/10.1149/1.2434690.
[32] S.J. Geng, J.H. Zhu, Z.G. Lu, Evaluation of several alloys for solid oxide fuel cell interconnect application, Scr. Mater. 55 (2006) 239–242.
[33] Z. Yang, J.S. Hardy, M.S. Walker, G. Xia, S.P. Simner, J.W. Stevenson, Structure and conductivity of thermally grown scales on ferritic Fe-Cr-Mn steel for SOFC interconnect applications, J. Electrochem. Soc. 151 (11) (2004) A1825, https://doi.org/10.1149/1.1797031.
[34] L. Blum, L.G.J. de Haart, J. Malzbender, N.H. Menzler, J. Remmel, R. Steinberger-Wilckens, Recent results in Jülich solid oxide fuel cell technology development, J. Power Sources 241 (2013) 477–485.
[35] S. Geng, Q. Zhao, Y. Li, J. Mu, G. Chen, F. Wang, S. Zhu, Sputtered MnCu metallic coating on ferritic stainless steel for solid oxide fuel cell interconnects application, Int. J. Hydrogen Energy 42 (2017) 10298–10307.
[36] S. Joshi, A. Petric, Nickel substituted $CuMn_2O_4$ spinel coatings for solid oxide fuel cell interconnects, Int. J. Hydrogen Energy 42 (2017) 5584–5589.
[37] Q. Zhao, S. Geng, G. Chen, F. Wang, Application of sputtered $NiFe_2$ alloy coating for SOFC interconnect steel, J. Alloy. Compd. 769 (2018) 120–129.
[38] Y. Pan, S. Geng, G. Chen, F. Wang, $CuFe_2O_4$/CuO coating for solid oxide fuel cell steel interconnects, Int. J. Hydrogen Energy 46 (44) (2021) 22942–22955.
[39] M. Zhao, S. Geng, G. Chen, F. Wang, FeCoNi converting coating for solid oxide fuel cell steel interconnect application, J. Power Sources 414 (2019) 530–539.
[40] Y.Z. Hu, Y.T. Su, C.X. Li, C.J. Li, G.J. Yang, Dense $Mn_{1.5}Co_{1.5}O_4$ coatings with excellent long-term stability and electrical performance under the SOFC cathode environment, Appl. Surf. Sci. 499 (2020) 143726.
[41] Y.Z. Hu, C.X. Li, C.J. Li, S.L. Zhang, Influence of pre-reduction on microstructure homogeneity and electrical properties of APS $Mn_{1.5}Co_{1.5}O_4$ coatings for SOFC interconnects, Int. J. Hydrogen Energy 42 (2017) 27241–27253.
[42] E. Zanchi, B. Talic, A.G. Sabato, S. Molin, A.R. Boccaccini, F. Smeacetto, Electrophoretic co-deposition of Fe_2O_3 and $Mn_{1.5}Co_{1.5}O_4$: processing and oxidation performance of Fe-doped Mn-Co coatings for solid oxide cell interconnects, J. Eur. Ceram. Soc. 39 (2019) 3768–3777.
[43] I. Thaheem, D.W. Joh, T. Noh, K.T. Lee, Highly conductive and stable $Mn_{1.35}Co_{1.35}Cu_{0.2}Y_{0.1}O_4$ spinel protective coating on commercial ferritic stainless steels for intermediate-temperature solid oxide fuel cell interconnect applications, Int. J. Hydrogen Energy 44 (2019) 4293–4303.
[44] Y.Z. Hu, C.X. Li, G.J. Yang, C.J. Li, Evolution of microstructure during annealing of $Mn_{1.5}Co_{1.5}O_4$ spinel coatings deposited by atmospheric plasma spray, Int. J. Hydrogen Energy 39 (2014) 13844–13851.
[45] S.J. Han, Z. Pala, S. Sampath, Plasma sprayed manganese-cobalt spinel coatings: process sensitivity on phase, electrical and protective performance, J. Power Sources 304 (2016) 234–243.
[46] F. Smeacetto, A. De Miranda, S. Cabanas Polo, S. Molin, D. Boccaccini, M. Salvo, A. R. Boccaccini, Electrophoretic deposition of $Mn_{1.5}Co_{1.5}O_4$ on metallic interconnect and interaction with glass-ceramic sealant for solid oxide fuel cells application, J. Power Sources 280 (2015) 379–386.
[47] B. Talic, S. Molin, K. Wiik, P.V. Hendriksen, H.L. Lein, Comparison of iron and copper doped manganese cobalt spinel oxides as protective coatings for solid oxide fuel cell interconnects, J. Power Sources 372 (2017) 145–156.
[48] M. Bednarz, S. Molin, M. Bobruk, M. Stygar, E. Długoń, M. Sitarz, T. Brylewski, High-temperature oxidation of the Crofer 22 H ferritic steel with $Mn_{1.45}Co_{1.45}Fe_{0.1}O_4$ and $Mn_{1.5}Co_{1.5}O_4$ spinel coatings under thermal cycling conditions and its properties, Mater. Chem. Phys. 225 (2019) 227–238.
[49] M. Zhao, S. Geng, G. Chen, F. Wang, Thermal conversion and evolution behavior of surface scale on SOFC interconnect steel with sputtered FeCoNi coating, Corros. Sci. 168 (2020) 108561.
[50] Z. Yang, G. Xia, X. Li, J. Stevenson, $(Mn, Co)_3O_4$ spinel coatings on ferritic stainless steels for SOFC interconnect applications, Int. J. Hydrogen Energy 32 (2007) 3648–3654.
[51] J.T. Gao, J.H. Li, Q.Y. Feng, C.J. Li, C.X. Li, High performance of ceramic current collector fabricated at 550 °C through in-situ joining of reduced $Mn_{1.5}Co_{1.5}O_4$ for metal-supported solid oxide fuel cells, Int. J. Hydrogen Energy 45 (2020) 29123–29130.
[52] N.H. Menzler, D. Sebold, O. Guillon, Post-test characterization of a solid oxide fuel cell stack operated for more than 30,000 hours: the cell, J. Power Sources 374 (2018) 69–76.
[53] Y.Z. Hu, C.X. Li, S.L. Zhang, G.J. Yang, X.T. Luo, C.J. Li, The microstructure stability of atmospheric plasma-sprayed $MnCo_2O_4$ coating under dual-atmosphere (H_2/Air) exposure, J. Therm. Spray Technol. 25 (2015) 301–310.
[54] A. Rabiei, A.G. Evans, Failure mechanisms associated with the thermally grown oxide in plasma-sprayed thermal barrier coatings, Acta Mater. 48 (2000) 3963–3976.
[55] D. Seo, K. Ogawa, Y. Nakao, H. Miura, T. Shoji, Influence of high-temperature creep stress on growth of thermally grown oxide in thermal barrier coatings, Surf. Coat. Technol. 203 (2009) 1979–1983.
[56] G. Pulci, J. Tirillò, F. Marra, F. Sarasini, A. Bellucci, T. Valente, C. Bartuli, High temperature oxidation of MCrAlY coatings modified by Al_2O_3 PVD overlay, Surf. Coat. Technol. 268 (2015) 198–204.
[57] L. Zhu, S. Zhu, F. Wang, J. Zhang, Comparison of the cyclic oxidation behavior of a low expansion Ni+CrAlYSiN nanocomposite and a NiCrAlYSi coating, Corrosion Sci. 80 (2014) 393–401.
[58] W.Z. Zhu, S.C. Deevi, Development of interconnect materials for solid oxide fuel cells, Mater. Sci. Eng., A 348 (1-2) (2003) 227–243.
[59] Y. Arata, A. Ohmori, C.-J. Li, Electrochemical method to evaluate the connected porosity in ceramic coatings, Thin Solid Films 156 (2) (1988) 315–326.
[60] H. Tsukuda, A. Notomi, N. Histatome, Application of plasma spraying to tubular-type solid oxide fuel cells production, J. Therm. Spray Technol. 9 (2000) 364–368.
[61] J. Malzbender, P. Batfalsky, R. Vaßen, V. Shemet, F. Tietz, Component interactions after long-term operation of an SOFC stack with LSM cathode, J. Power Sources 201 (2012) 196–203.